OEA | Opto-Electronic Advances

Smart reconfigurable metadevices made of shape memory alloy metamaterials

Shiqiang Zhao, Yuancheng Fan*, Ruisheng Yang, Zhehao Ye, Fuli Zhang*, Chen Wang, Weijia Luo, Yongzheng Wen*, Ji Zhou*

https://doi.org/10.29026/oea.2025.240109

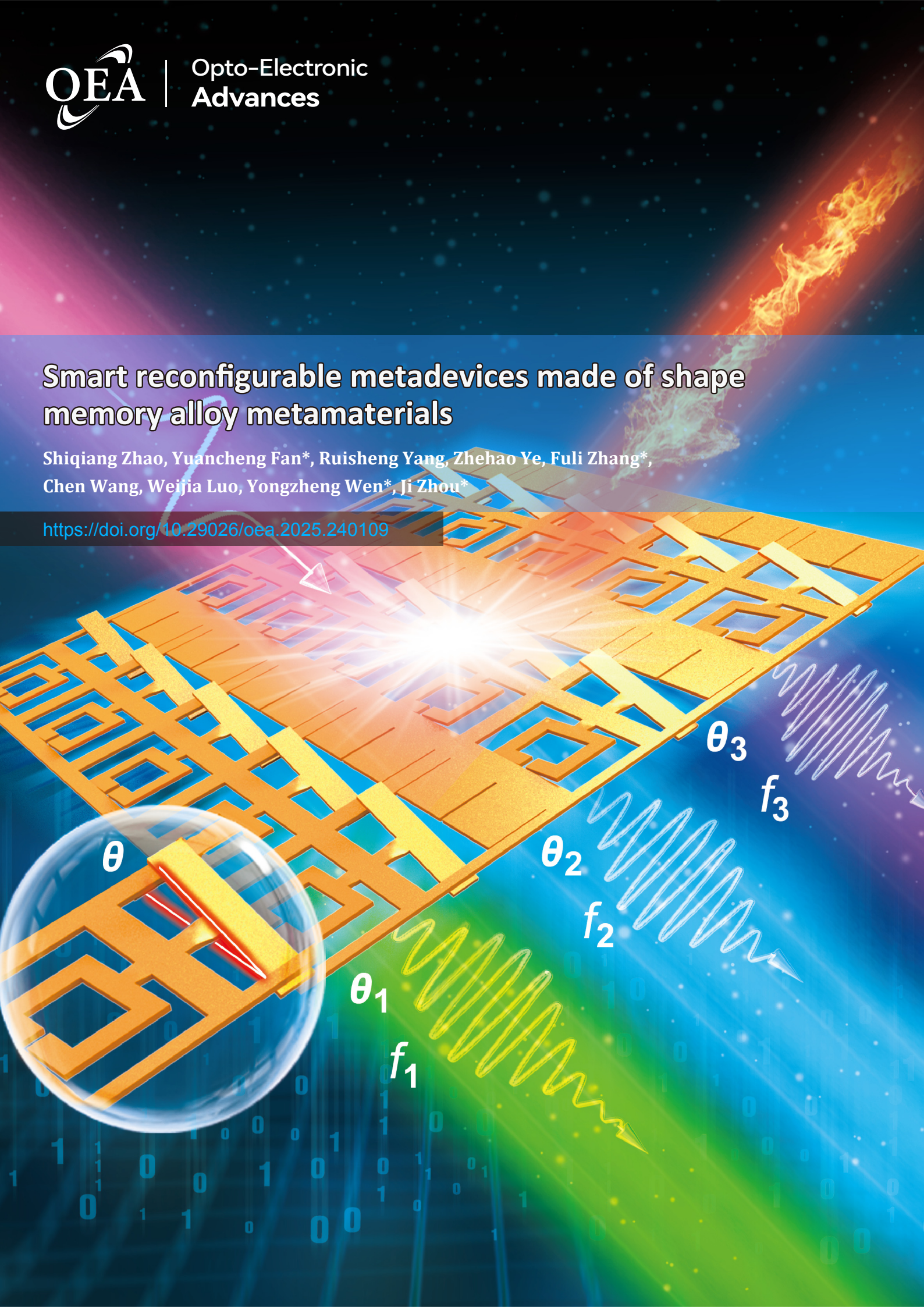

Opto-Electronic Advances

CN 51–1781/TN ISSN 2096–4579 (Print) ISSN 2097–3993 (Online)

Smart reconfigurable metadevices made of shape memory alloy metamaterials

Shiqiang Zhao, Yuancheng Fan, Ruisheng Yang, Zhehao Ye, Fuli Zhang, Chen Wang, Weijia Luo, Yongzheng Wen and Ji Zhou

Citation: Zhao SQ, Fan YC, Yang RS, et al. Smart reconfigurable metadevices made of shape memory alloy metamaterials. *Opto-Electron Adv* **8**, 240109(2025).

https://doi.org/10.29026/oea.2025.240109

Received: 10 May 2024; Accepted: 28 August 2024; Published online: 3 January 2025

Opto-Electronic Advances

Article

February 2025, Vol. 8, No. 2

DOI: 10.29026/oea.2025.240109 CSTR: 32247.14.oea.2025.240109

Smart reconfigurable metadevices made of shape memory alloy metamaterials

Shiqiang Zhao[1,2], Yuancheng Fan[1*], Ruisheng Yang[1], Zhehao Ye[1], Fuli Zhang[1*], Chen Wang[2], Weijia Luo[2], Yongzheng Wen[2*] and Ji Zhou[2*]

Reconfigurable metamaterials significantly expand the application scenarios and operating frequency range of metamaterials, making them promising candidates for use in smart tunable device. Here, we propose and experimentally demonstrate that integrating metamaterial design principles with the intrinsic features of natural materials can engineer thermal smart metadevices. Tunable extraordinary optical transmission like (EOT-like) phenomena have been achieved in the microwave regime using shape memory alloy (SMA). The strongly localized fields generated by designed metadevices, combined with the intense interference of incident waves, enhance transmission through subwavelength apertures. Leveraging the temperature-responsive properties of SMA, the morphology of the metadevice can be recontructed, thereby modifying its response to electromagnetic waves. The experiments demonstrated control over the operating frequency and transmission amplitude of EOT-like behavior, achieving a maximum transmission enhancement factor of 126. Furthermore, the metadevices with modular design enable the realization of multiple functions with independent control have been demonstrated. The proposed SMA-based metamaterials offer advantages in terms of miniaturization, easy processing, and high design flexibility. They may have potential applications in microwave devices requiring temperature control, such as sensing and monitoring.

Keywords: metamaterials; extraordinary optical transmission; shape memory alloy; temperature tunability

Zhao SQ, Fan YC, Yang RS et al. Smart reconfigurable metadevices made of shape memory alloy metamaterials. *Opto-Electron Adv* **8**, 240109 (2025).

Introduction

Over the past decade, there has been rapid development in metamaterials across various fields such as physics, materials science, and electrocommunication, driven by the resonant characteristics of artificial elements[1–6]. Due to limitations in manufacturing and performance uniformity, three-dimensional metamaterials are constrained in practical applications[7,8]. In contrast, two-dimensional (2D) metamaterials, also known as metasurfaces[9,10], with mature fabrication processes and ultra-thinness, hold broader application prospects, such as in antennas[11], sensors[12,13], lenses[14–16], imaging[17,18], and others. To overcome the limitation of static operating mode, tunable metamaterials have been proposed, encompassing electrical, magnetic, and mechanical mechanisms[19–23]. Recently, thermal tunable metamaterials have provided an effective platform for thermal management engineering[24–26]. These methods enable thermal dynamic responses from

[1]MOE Key Laboratory of Material Physics and Chemistry under Extraordinary Conditions, School of Physical Science and Technology, Northwestern Polytechnical University, Xi'an 710129, China; [2]State Key Lab of New Ceramics and Fine Processing, Department of Materials Science and Engineering, Tsinghua University, Beijing 100084, China.

*Correspondence: YC Fan, E-mail: phyfan@nwpu.edu.cn; FL Zhang, E-mail: fuli.zhang@nwpu.edu.cn; YZ Wen, E-mail: wenyzheng@tsinghua.edu.cn; J Zhou, E-mail: zhouji@tsinghua.edu.cn

Received: 10 May 2024; Accepted: 28 August 2024; Published online: 3 January 2025

radio frequency to visible light and have made progress[27–30]. However, the complexity of structures and materials limits the design flexibility of devices, hindering their practical application prospects. Shape memory alloy (SMA) is a type of temperature phase transition material[31,32]. These materials undergo phase changes in response to different thermal stimuli and can transform into one another, resulting in a macroscopic shape memory effect (SME)[33,34]. The temperature-reconfigurable properties of SMA may provide a promising platform for developing thermal-tunable devices, overcoming previous challenges.

The extraordinary optical transmission (EOT) through subwavelength apertures has become a research hotspot due to the underlying physical mechanisms and the promising applications in high-resolution imaging[35,36]. According to Bethe's theoretical analysis[37], the transmission with λ through a single subwavelength aperture of radius r will decrease rapidly in the form $(r/\lambda)^4$. A seminal work revealed that EOT occurs at specific frequency when the light impacts on a plate filled with an array of subwavelength holes[38]. Although EOT could be achieved in early work, the larger device dimensions limited the integration of photonic devices[39–41]. Moreover, the EOT derived from surface plasmon polariton (SPP) is typically realized in the visible light due to the optical properties of metals. However, a theoretical report predicted the existence of localized surface plasmon mode induced by artificial structure, known as spoof surface plasmon polariton (SSPP)[42], which exhibits similar dispersion behavior to SPP. The SSPP is not restricted by the metals' inherent plasma frequency and can be achieved in the microwave band since it originates from artificially engineering structures. Subsequent work demonstrated that strong localized resonance mode of metamaterials can interacting with the subwavelength apertures in metals for exhibiting extraordinary optical transmission like (EOT-like) behavior[43–45]. However, in existing reports, the operating frequency of the device is typically fixed, limiting its further development in practical applications.

In this work, we propose the construction of metadevices based on Ti-Ni shape memory alloy to achieve tunable EOT-like response. For a subwavelength aperture of $\lambda/6$ (λ is vacuum wavelength), the designed metadevice can achieve a 126-fold transmission enhancement, with a maximum transmission rate exceeding 90%. Designed two types of device structures are split resonant ring (SRR) and long-stick structure, corresponding to narrowband and broadband responses, respectively. Temperature excitation can drive the metadevice to undergo structural reconfiguration, thereby enabling intelligent control of the operating frequency and transmission amplitude of EOT-like behavior. The combination of dual structures reveals that independent control of two operating frequency points can be achieved by designing metamaterial structures. Experimental results demonstrated that the fusion of metamaterials and natural materials can achieve performance tailored to specific requirements. The designed metadevice, due to its simple fabrication process, compact structural dimensions, high design freedom, and tunable performance, provides an intelligent device for communication, sensing, and so on.

Results and discussion

The schematic is shown in Fig. 1. The material used in this work is Ti-Ni SMA with thermoelastic martensitic phase transition (The details can be seen in the Section 1 of Supplementary information). When stress is applied to SMA at temperatures equivalent to room temperature, the strain in SMA persists even after unloading the stress. As the temperature rises, the stored strain in SMA is released, leading to a macroscopic change in shape. Specifically, due to the reversible nature of the crystallography in SMA, when the temperature exceeds the phase transition point, the martensitic phase undergoes a reverse transformation along the original shear path, returning to the lattice orientation of the parent phase. This imparts SME characteristics to SMA. Leveraging the inherent material properties that temperature-induced macroscopic shape changes, we can construct shape-reconfigurable thermal smart devices. Figure 1(a) illustrates two typical types of shape memory effects. For SMA exhibiting one-way shape memory effect (O-SMA), deformation disappears upon cooling but does not reconstruct upon returning to the high-temperature phase. For SMA with two-way shape memory effect (T-SMA), deformation and recovery are reversible, meaning that macroscopic deformation can reconstruct upon returning to the high-temperature phase. These properties are closely related to the material characteristics and post-processing of SMA themselves.

Figure 1(b) illustrates the two types of metadevices designed to achieve customizable performance for tunable EOT-like behavior. The metadevices fabricated from

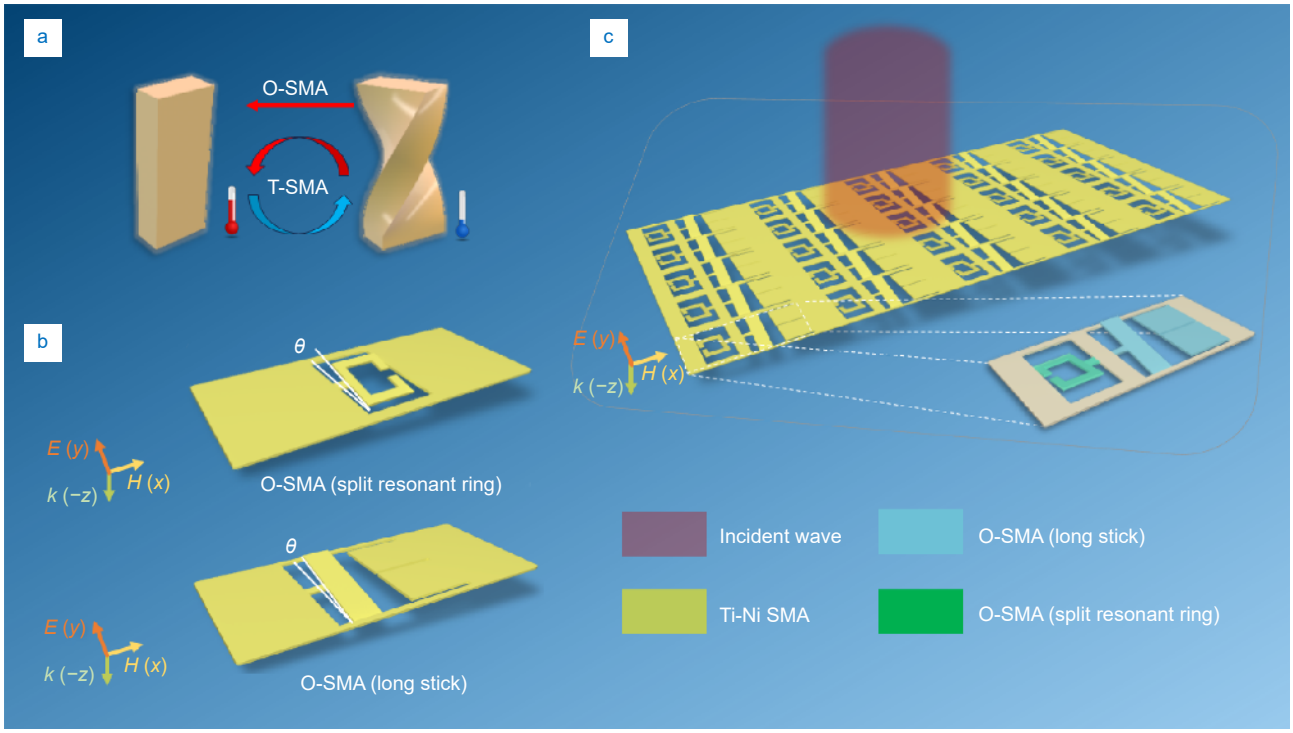

Fig. 1 | Schematic function tunability with temperature and designs of the smart metadevices. (**a**) O-SME: one-way shape memory effect; T-SME: two-way shape memory effect. (**b**) and (**c**) To demonstrate the concept, three devices are designed.

SMA integrate two properties: electromagnetic response and temperature response. Based on the narrowband response characteristic of magnetic dipole resonant modes, we designed metadevices utilizing split resonant ring (SRR)[46]. Upon excitation by an electric field, circular oscillating currents can be induced on the metal rings, thereby eliciting magnetic dipole resonant modes. Since the induced magnetic field is perpendicular to the incident magnetic field, it cannot couple with the magnetic field of the incident wave to form the dark state[47]. As a demonstration of customizable performance, a long stick model based on electric dipole resonant modes was designed. Such modes directly interact with the incident electric field, are commonly referred to as bright modes and exhibit broadband responses. Under the excitation of a temperature field, both models undergo deformation, leading to the restruction of the metadevices relative to the orientation of the incident wave. This restruction directly affects the coupling frequency and intensity, enabling dual control over the transmission peak frequency and amplitude.

To demonstrate the exceptional design freedom of metamaterial-based devices, Fig. 1(c) presents a dual-band metamaterial model. By integrating the narrowband and broadband models into one metamaterial device, it becomes possible to simultaneously achieve two functionalities. Through independent temperature control of the dual-band model, it becomes feasible to exert independent control over both operating modes, including their working frequency points and transmission amplitudes. Metamaterials introduce on-demand design capabilities to device engineering, inspiring us to achieve more complex functionalities through modular engineering. To meet a wider range of application needs, in addition to demonstrating metamaterial functionality within waveguides, we also showcase numerical simulation results of periodic arrays in free space. It is worth mentioning that, beyond the cases presented in this work, the proposed strategy can be easily extended to accommodate a wider range of functionalities, providing a platform for designing novel thermally tunable devices.

Figure 2(a) illustrates the schematic diagram of the tunable metadevice. The interaction between the fields generated by metamaterials and incident waves exhibits a passband property at the resonant frequency, resulting in the maximum enhancement of transmittance. Equivalent circuit analysis aids in understanding the resonant behavior. The metallic components constituting the metadevice can be considered as resistors and inductors, while the air gaps can be viewed as capacitors. Based on

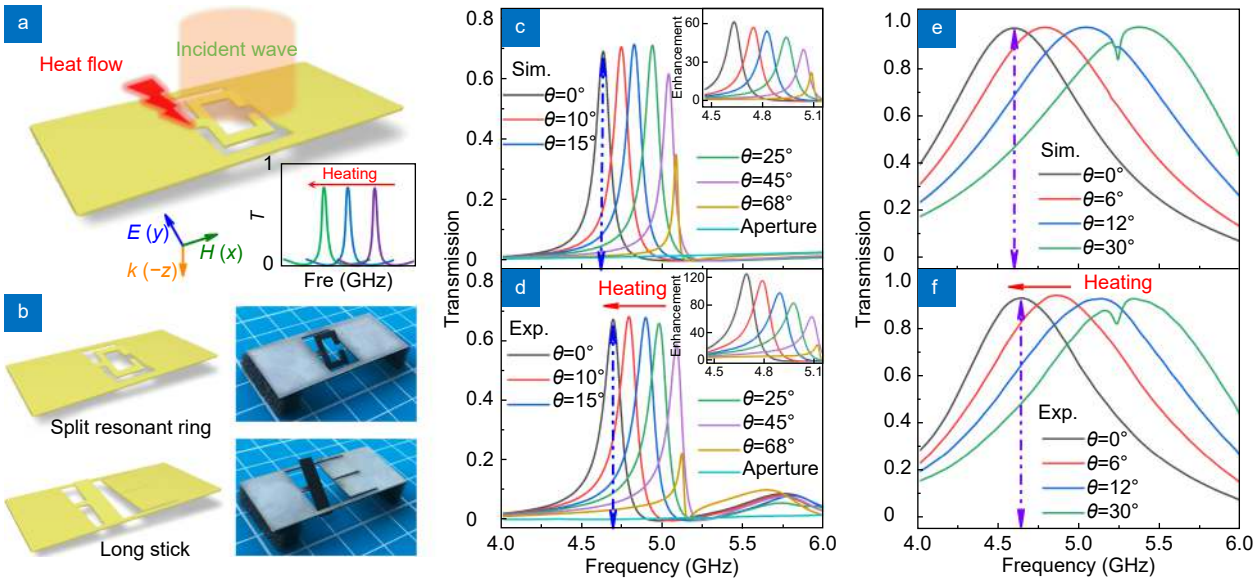

Fig. 2 | Experimental verification of tunable EOT-like behavior. (**a**) Illustration of thermal tunable metadevices with EOT-like response in C-band. (**b**) Schematics and samples of two metadevices. (**c**) and (**e**) are simulated, (**d**) and (**f**) are measured transmission results for SRR and long stick structure, respectively. Insets of (c) and (d) plot enhancement factor for models in (b).

the spatial relationships of these equivalent circuit elements, an equivalent circuit diagram corresponding to the metamaterial device can be constructed. At the resonance, the circuit achieves maximum passband properties. The geometry parameters can be seen in the Section 2 of Supplementary information.

The incident electromagnetic wave, polarized in the *y*-direction, interacts with the designed metadevice, inducing enhanced localized fields within the SRR at its resonant frequency, thereby facilitating the transmission of electromagnetic waves through subwavelength apertures. Under the influence of an external temperature field, the angle θ between the plane containing the SRR and the plane of the metal plate changes. This alteration results in a macroscopic change in the morphology of the metadevice, thereby affecting its electromagnetic response characteristics and achieving tunable EOT-like behavior. The proposed metamaterial route was used to achieve EOT-like response at C-band as an experimental verification. We prepared the samples using laser cutting technology. Compared to the fabrication process of phase-change materials or bimaterial cantilevers, this manufacturing process is a one-step procedure, offering the advantages of convenience, low cost, and rapid preparation. Figure 2(b) displays the samples of the narrowband and broadband models operating in the waveguide environment, which match the design well.

We utilized the finite difference time domain (FDTD) method to simulate the electromagnetic response of the designed metadevices. The simulation frequency range was set from 4 to 6 GHz. The simulation environment was configured as a waveguide environment, with corresponding boundary conditions: electric boundaries along the *x* and *y* directions, and open boundaries along the *z* direction. In the simulation, the SMA was defined as a lossy metallic material with a conductivity of 1×10^6 S/m[48], and a thickness of 0.5 mm. The angle θ between the metamaterial resonant structure and the metal plane was set as a variable in the simulation. Transmission data of the metadevices at different angles θ were obtained through the simulation. The more details can be seen in the Section 3 of Supplementary information.

The numerical results are shown in Fig. 2(c) and 2(e), corresponding to the narrowband and broadband models in Fig. 2(b), respectively. The solid cyan line in Fig. 2(c) is the transmission spectrum of metadevice only with a subwavelength aperture of 11.90×10.58 mm^2 without the SRR inside. For a single subwavelength aperture, the transmission of the entire frequency band is awfully weak, below 2%. However, when SRRs are introduced into such a subwavelength aperture, a significant enhancement of the transmission wave can be observed at the resonance frequency in the simulation, reaching about 70%, as shown by the black solid line in Fig. 2(c). For θ = 0°, the transmission peak frequency appears at 4.63 GHz and 4.60 GHz, and the transmission is 69.1% and 97.1%

for the narrowband and broadband models in the simulations, respectively. The simulation results demonstrate that the designed metamaterial structure can effectively enhance the transmission of electromagnetic waves through subwavelength apertures. The simulated transmission bandwidths are 80 MHz and 1060 MHz, corresponding to the narrowband and broadband models, respectively. As expected, the metadevices designed based on different coupling characteristics exhibit distinct electromagnetic response characteristics.

In the experimental measurements, we employed the vector network analyzer AV3629D as the signal generating device. The sample was placed in the waveguide WR-187 that is connected to the vector network via a coaxial line. The experimental setup can be seen in Section 4 of Supplementary information. The excitation mode was TE_{10} main mode and the measured results are shown in Fig. 2(d) and 2(f). For $\theta = 0°$, the experimental transmission peak frequency appears at 4.69 GHz and 4.64 GHz, and the transmission is 67.0% and 93.0% for the narrowband and broadband models in the simulations, respectively. The measured results are in good agreement with simulated ones. Due to their higher quality factor, narrowband models exhibit greater enhancement in the localized field, resulting in higher ohmic losses. Therefore, compared to broadband models, narrowband models show lower measured transmission in experiments. The detail absorption value can be seen in Section 4 of Supplementary information. The measured transmission bandwidths are 120 MHz and 1010 MHz, corresponding to the narrowband and broadband models, respectively. The insets in Fig. 2(c) and 2(d) show the transmission enhancement factor, which was defined as the ratio of the transmission of TE_{10} wave through a metadevice to that through the aperture only. For a subwavelength (about $\lambda/6$: λ is vacuum wavelength) aperture, the experiment achieved a maximum transmission enhancement of up to 126-fold. The experimental results are consistent with the expectations, demonstrating the crucial role of metamaterials in achieving EOT-like response.

A temperature field of 55 °C is introduced to alter the macroscopic morphology of the metadevice, thereby demonstrating tunable EOT-like. The illustration in Fig. 2(c) and 2(e) depict the simulations of the changes in operating frequency and amplitude of EOT-like peak at different angles. It is evident that as the angle θ decreases, the resonant frequency of the metadevice undergoes a redshift towards lower frequencies. This is attributed to the morphological changes in the metadevice, leading to alterations in the equivalent circuit. Additionally, we observe that, at a fixed operating frequency, the amplitude of EOT-like transmission peak can be effectively controlled as the angle θ varies, as indicated by the dashed arrows in Fig. 2(c) and 2(e). For the experiments, during the heating process in a temperature-controlled box of 55 °C, the angle θ gradually decreases from its maximum value to zero. We measured experimental data for several representative angles, as shown in Fig. 2(d) and 2(f). As the temperature-driven SMA undergoes deformation, its response to electromagnetic waves also changes, including resonance frequency and transmission amplitude. The experimental results are in good agreement with the simulations, demonstrating the feasibility of SMA in realizing thermally tunable smart devices. An anomalous transmission curve has been observed in both simulations and experiments in broadband models. This arises from the trapped mode[49] induced by morphological changes, resulting in an anomalous transmission Strough. More details can be seen in Section 5 of Supplementary information.

To further elucidate the performance of the metadevices, we analyze the tunability of the operating frequency and transmission amplitude. Figure 3(a) illustrates the performance of the narrowband model based on SRR. We can obtain a measured modulation in transmission from 3.6% to 67.0% at 4.69 GHz, with the transmission peak frequency shifting from 5.12 GHz to 4.69 GHz as the angle θ changes driven by temperature. Similar results of the broadband model are shown in the Fig. 3(b). When the temperature-driven angle θ of the long stick changes, modulation of the transmittance ranging from 48.6% to 93.0% can be achieved, with modulation of the transmission peak frequency from 5.33 GHz to 4.64 GHz. In the process of achieving tunable EOT-like behavior, both the narrowband model and the broadband model retain their corresponding bandwidths, approximately 120 MHz and 1010 MHz, respectively. In theory, we can achieve continuous tunability by continuously changing the angle θ through temperature control. Such tunability holds potential for applications in temperature sensing and tunable communication filtering scenarios[50,51].

Numerical simulations of field distributions on metadevices are beneficial for understanding the mechanisms behind resonance. We calculated the distribution of the surface currents as shown in the Fig. 3(c) and 3(d),

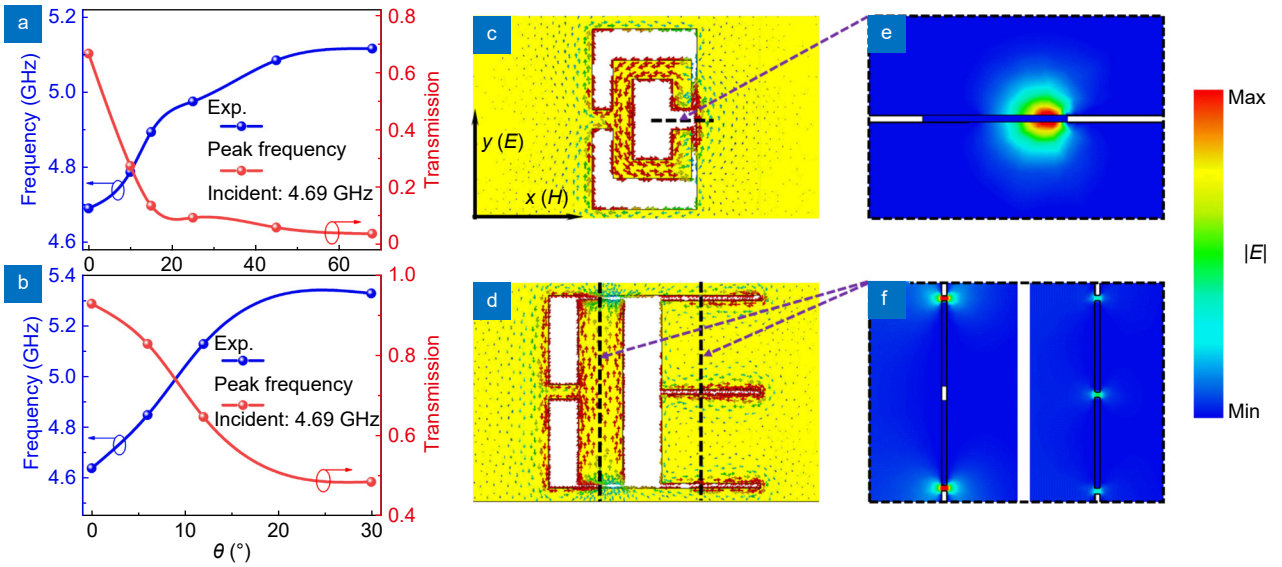

Fig. 3 | The control over the operating frequency and amplitude of EOT-like peak and near-field distribution. (**a**) and (**b**) show the tunable abilities of proposed metadevice for operating frequency and transmission amplitude. (**c–f**) Schematic of distribution of simulated currents and electric fields for SRR and long stick model. External excitation electric field induced a ring current for SRR, while a dipole current for long stick model. Such current distribution leads to electric field distribution in (e) and (f).

and electric fields as shown in the Fig. 3(e) and 3(f) at resonant frequencies. As anticipated, the circulatory surface currents on the SRR confirmed its magnetic dipole resonance mode, while the dipole currents on the long stick confirmed its electric dipole resonance mode. The distribution of the electric field also aligns with expectations, with strong localized fields supporting the analysis of equivalent circuit models. There are significant electric field maxima at the locations of the equivalent capacitors. The scattering field of the metadevice, coupled with incident interference, leads to the EOT-like phenomenon.

Finally, we integrate the narrowband and broadband models into one metadevice to demonstrate the advantages of functional scalability. Through careful design of the dimensions of the metamaterial structure, we have achieved a dual-band model, and the details can be seen in the Section 6 of Supplementary information. The numerical simulation results in Fig. 4(b) and 4(d) demonstrate that independently adjusting the angles θ of the SRR and long stick structures enables independent control of the operating frequencies and transmission amplitudes. In the experiments, we independently adjusted the structure using a heated air gun. Figure 4(a) and 4(c) illustrate the independent modulation of EOT-like response at different operating frequency points. The experiments demonstrate that it is possible to modulate the correlated properties of EOT-like response for the one mode while maintaining the operating frequency and intensity of the other mode unchanged. In addition to the metadevices demonstrated in the waveguide environment, Fig. 4(e) illustrates the formation of metasurfaces composed of these metadevices. Tunable metasurfaces offer broader application scenarios in free-space environments. Figure 4(f) presents simulated transmission spectra results, elucidating the EOT-like phenomenon of the dual-band model. Modular and flexible combinations provide thermal tunable devices with increased design flexibility, enabling adaptation to complex scenarios and meeting the demands of multifunctional integration[52]. Notably, thanks to the highly customizable nature of metamaterials, the proposed strategy is not limited to operating in the microwave band. By scaling the geometric dimensions of the metamaterials, it is promising to extend the frequency range to the terahertz band. Developing tunable metamaterial devices in terahertz range holds significant scientific and engineering value[53,54].

Figure 5 demonstrates the independent control capability of the dual-band model on transmission. The two operating frequencies are denoted as f_1 (4.24 GHz) and f_2 (5.29 GHz), corresponding to the SRR and long stick structures, respectively. When the temperature drives changes in the SRR structure while keeping the long stick structure unchanged, it can be observed that the transmission at f_1 decreases from 67.2% to 10.6%, while the

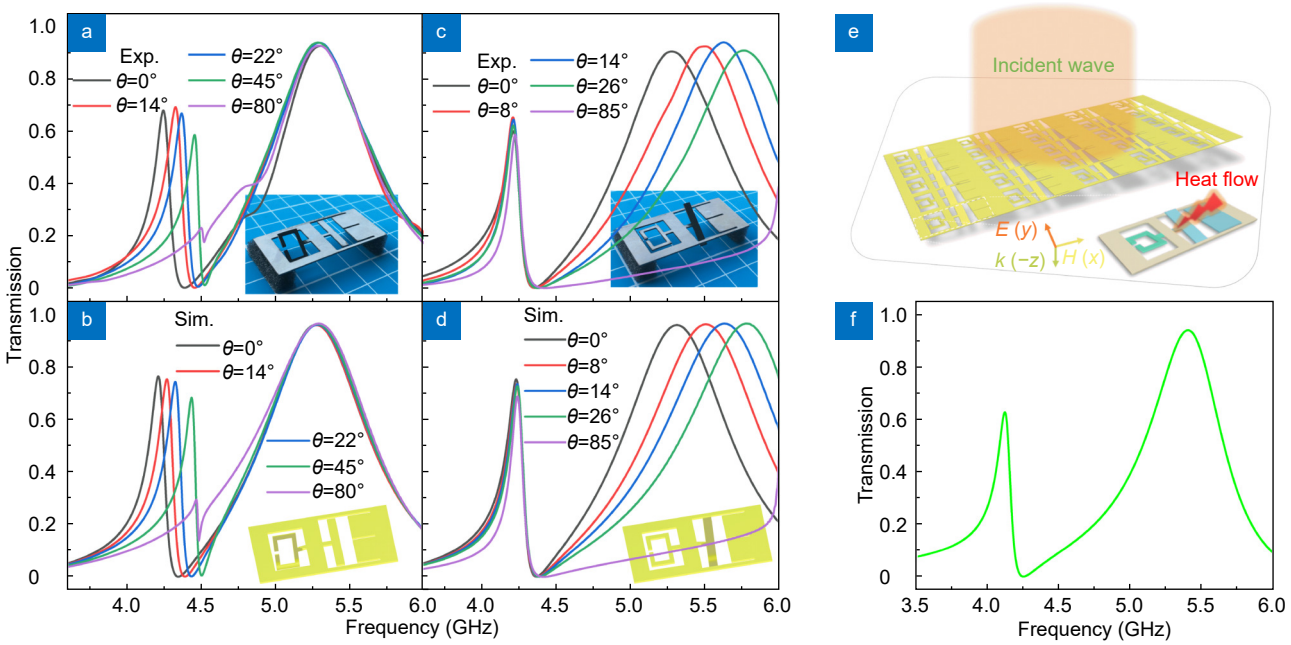

Fig. 4 | Dual-band and periodic model. (**a**) and (**c**) are measured, (**b**) and (**d**) are simulated transmission results for left-pass and right-pass independent, respectively. (**e**) The concept that the SRR is extended to form metasurfaces. (**f**) Under the same polarized electromagnetic signal, the metasurfaces made of SRR possess identical performance with metadevice working in waveguide.

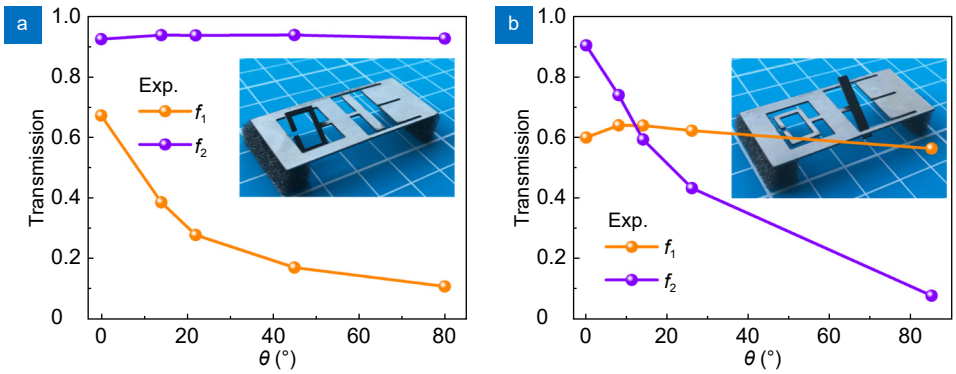

Fig. 5 | Independent transmission modulation of the dual-band model. (**a**) and (**b**) are measured independent transmission modulation results for left-pass (operating frequency: f_1) and right-pass (operating frequency: f_2), respectively.

transmission at f_2 remains above 90% (Fig. 5(a)). Conversely, when the temperature drives changes in the long stick structure while keeping the SRR unchanged, control over the transmission at f_2, varying from 90.4% to 7.6%, can be achieved, while maintaining the transmission at f_1 above 60% (Fig. 5(b)). We simulated the impact of the distance between two elements on transmission and found that a smaller distance leads to lower losses, resulting in a slight increase in transmission, the details can be seen in the Section 6 of Supplementary information. The results indicate that metamaterials based on SMA provide a new strategy for realizing EOT devices with simultaneous modulation at multiple frequency points.

Conclusions

In summary, we have proposed and experimentally verified the concept of utilizing SMA to construct thermal intelligent reconfigurable metadevices. Narrowband and broadband models were developed based on SRR and long stick structures, with measured response bandwidths of 120 MHz and 1010 MHz, respectively. The interference between the scattered waves of the metadevices and incident waves enables EOT-like response through subwavelength apertures, with a maximum experimental enhancement factor of 126. The temperature-tunable capability of SMA enables modulation of the operating frequency and transmission amplitude for

EOT-like peak. Under excitation at 55 °C, deformation angles θ exceeding 80° were achieved, resulting in frequency shifts of over 700 MHz and 60% modulation of transmission amplitude. Furthermore, leveraging the highly designable properties of metamaterials, the narrowband and broadband models are integrated into one metadevice, forming the dual-band model. This combined model enables independent control over multiple frequency points. The proposed pathway of SMA-based metamaterials offers advantages such as convenient processing, high design flexibility, and miniaturization, and can be easily extended to other thermally related fields and frequency bands, including MEMS, thermo-mechanics and thermo-optical coupling.

Experimental section

Our samples can be processed by laser cutting technology of one-time forming using a 0.5 mm thick Ti-Ni commercial SMA sheet. To avoid damaging the SME of SMA due to processing temperatures, we conducted a heat treatment process after completing the sample fabrication. The SMA samples were placed in a muffle furnace with an air atmosphere at 500 °C for an hour. Subsequently, the furnace was turned off, and after four hours, the samples were cooled to 200 °C before being removed and allowed to air-cool to room temperature. We also employ line cutting technology for processing, which offers the advantage of avoiding localized high temperatures at the cutting location. However, compared to laser cutting technology, it requires more time. In our measurement, the sample is placed in WR-187 rectangular waveguide with dimensions of 22.15×47.55 mm^2, and is measured by a vector network analyzer (AV3629D). The heating process is carried out by a temperature control box, and the deformation angle θ is measured with a protractor after heating is ceased.

References

1. Hess O, Pendry JB, Maier SA et al. Active nanoplasmonic metamaterials. *Nat Mater* **11**, 573–584 (2012).
2. Kadic M, Milton GW, van Hecke M et al. 3D metamaterials. *Nat Rev Phys* **1**, 198–210 (2019).
3. Kruk SS, Wong ZJ, Pshenay-Severin E et al. Magnetic hyperbolic optical metamaterials. *Nat Commun* **7**, 11329 (2016).
4. Liu N, Guo HC, Fu LW et al. Three-dimensional photonic metamaterials at optical frequencies. *Nat Mater* **7**, 31–37 (2008).
5. Shelby RA, Smith DR, Schultz S. Experimental verification of a negative index of refraction. *Science* **292**, 77–79 (2001).
6. Zheludev NI, Kivshar YS. From metamaterials to metadevices. *Nat Mater* **11**, 917–924 (2012).
7. Soukoulis CM, Wegener M. Past achievements and future challenges in the development of three-dimensional photonic metamaterials. *Nat Photonics* **5**, 523–530 (2011).
8. Yang FB, Zhang ZR, Xu LJ et al. Controlling mass and energy diffusion with metamaterials. *Rev Mod Phys* **96**, 015002 (2024).
9. Arbabi A, Arbabi E, Horie Y et al. Planar metasurface retroreflector. *Nat Photonics* **11**, 415–420 (2017).
10. Lee GY, Hong JY, Hwang SH et al. Metasurface eyepiece for augmented reality. *Nat Commun* **9**, 4562 (2018).
11. Wu GB, Dai JY, Shum KM et al. A universal metasurface antenna to manipulate all fundamental characteristics of electromagnetic waves. *Nat Commun* **14**, 5155 (2023).
12. Qin J, Jiang SB, Wang ZS et al. Metasurface micro/nano-optical sensors: principles and applications. *ACS Nano* **16**, 11598–11618 (2022).
13. Wang YL, Zhao C, Wang JJ et al. Wearable plasmonic-metasurface sensor for noninvasive and universal molecular fingerprint detection on biointerfaces. *Sci Adv* **7**, eabe4553 (2021).
14. Lin DM, Fan PY, Hasman E et al. Dielectric gradient metasurface optical elements. *Science* **345**, 298–302 (2014).
15. Wang FL, Zhao SQ, Wen YZ et al. High efficiency visible achromatic metalens design via deep learning. *Adv Opt Mater* **11**, 2300394 (2023).
16. Wang Q, Zhang XQ, Xu YH et al. A broadband metasurface-based terahertz flat-lens array. *Adv Opt Mater* **3**, 779–785 (2015).
17. High AA, Devlin RC, Dibos A et al. Visible-frequency hyperbolic metasurface. *Nature* **522**, 192–196 (2015).
18. Zheng GX, Mühlenbernd H, Kenney M et al. Metasurface holograms reaching 80% efficiency. *Nat Nanotechnol* **10**, 308–312 (2015).
19. Chen HT, Padilla WJ, Cich MJ et al. A metamaterial solid-state terahertz phase modulator. *Nat Photonics* **3**, 148–151 (2009).
20. Kang L, Cui YH, Lan SF et al. Electrifying photonic metamaterials for tunable nonlinear optics. *Nat Commun* **5**, 4680 (2014).
21. Ma CP, Wu S, Ze QJ et al. Magnetic multimaterial printing for multimodal shape transformation with tunable properties and shiftable mechanical behaviors. *ACS Appl MaterInterfaces* **13**, 12639–12648 (2021).
22. Montgomery SM, Wu S, Kuang X et al. Magneto-mechanical metamaterials with widely tunable mechanical properties and acoustic bandgaps. *Adv Funct Mater* **31**, 2005319 (2021).
23. Shrekenhamer D, Chen WC, Padilla WJ. Liquid crystal tunable metamaterial absorber. *Phys Rev Lett* **110**, 177403 (2013).
24. Kats MA, Blanchard R, Genevet P et al. Thermal tuning of mid-infrared plasmonic antenna arrays using a phase change material. *Opt Lett* **38**, 368–370 (2013).
25. Lewandowski W, Fruhnert M, Mieczkowski J et al. Dynamically self-assembled silver nanoparticles as a thermally tunable metamaterial. *Nat Commun* **6**, 6590 (2015).
26. Tao H, Strikwerda AC, Fan K et al. Reconfigurable terahertz metamaterials. *Phys Rev Lett* **103**, 147401 (2009).
27. Degiron A, Mock JJ, Smith DR. Modulating and tuning the response of metamaterials at the unit cell level. *Opt Express* **15**, 1115–1127 (2007).
28. Driscoll T, Kim HT, Chae BG et al. Memory metamaterials. *Science* **325**, 1518–1521 (2009).
29. Ou JY, Plum E, Jiang L et al. Reconfigurable photonic metamaterials. *Nano Lett* **11**, 2142–2144 (2011).
30. Wang WH, Srivastava YK, Gupta M et al. Photoswitchable

anapole metasurfaces. *Adv Opt Mater* **10**, 2102284 (2022).
31. Buehler WJ, Gilfrich JV, Wiley RC. Effect of low‐temperature phase changes on the mechanical properties of alloys near composition TiNi. *J Appl Phys* **34**, 1475–1477 (1963).
32. Ölander A. An electrochemical investigation of solid cadmium-gold alloys. *J Am Chem Soc* **54**, 3819–3833 (1932).
33. Chluba C, Ge WW, Lima de Miranda R et al. Ultralow-fatigue shape memory alloy films. *Science* **348**, 1004–1007 (2015).
34. Ueland SM, Chen Y, Schuh CA. Oligocrystalline shape memory alloys. *Adv Funct Mater* **22**, 2094–2099 (2012).
35. Baskourelos K, Tsilipakos O, Stefański T et al. Topological extraordinary optical transmission. *Phys Rev Res* **4**, L032011 (2022).
36. Brolo AG. Plasmonics for future biosensors. *Nat Photonics* **6**, 709–713 (2012).
37. Bethe HA. Theory of diffraction by small holes. *Phys Rev* **66**, 163–182 (1944).
38. Ebbesen TW, Lezec HJ, Ghaemi HF et al. Extraordinary optical transmission through sub-wavelength hole arrays. *Nature* **391**, 667–669 (1998).
39. Lezec HJ, Thio T. Diffracted evanescent wave model for enhanced and suppressed optical transmission through subwavelength hole arrays. *Opt Express* **12**, 3629–3651 (2004).
40. Liu HT, Lalanne P. Microscopic theory of the extraordinary optical transmission. *Nature* **452**, 728–731 (2008).
41. Martín-Moreno L, García-Vidal FJ, Lezec HJ et al. Theory of extraordinary optical transmission through subwavelength hole arrays. *Phys Rev Lett* **86**, 1114–1117 (2001).
42. Pendry JB, Martín-Moreno L, Garcia-Vidal FJ. Mimicking surface plasmons with structured surfaces. *Science* **305**, 847–848 (2004).
43. Aydin K, Cakmak AO, Sahin L et al. Split-ring-resonator-coupled enhanced transmission through a single subwavelength aperture. *Phys Rev Lett* **102**, 013904 (2009).
44. Chen WC, Landy NI, Kempa K et al. A subwavelength extraordinary-optical-transmission channel in babinet metamaterials. *Adv Opt Mater* **1**, 221–226 (2013).
45. Navarro-Cía M, Beruete M, Campillo I et al. Enhanced lens by ε and μ near-zero metamaterial boosted by extraordinary optical transmission. *Phys Rev B* **83**, 115112 (2011).
46. Smith DR, Padilla WJ, Vier DC et al. Composite medium with simultaneously negative permeability and permittivity. *Phys Rev Lett* **84**, 4184–4187 (2000).
47. Yang YM, Kravchenko II, Briggs DP et al. All-dielectric metasurface analogue of electromagnetically induced transparency. *Nat Commun* **5**, 5753 (2014).
48. Wu SK, Lin HC, Lin TY. Electrical resistivity of Ti–Ni binary and Ti–Ni–X (X= Fe, Cu) ternary shape memory alloys. *Mater Sci Eng A* **438–440**, 536–539 (2006).
49. Fedotov VA, Rose M, Prosvirnin SL et al. Sharp trapped-mode resonances in planar metamaterials with a broken structural symmetry. *Phys Rev Lett* **99**, 147401 (2007).
50. Li WC, Wang Y, Chen T et al. Algorithmic encoding of adaptive responses in temperature-sensing multimaterial architectures. *Sci Adv* **9**, eadk0620 (2023).
51. Wang QH, Gao BT, Raglione M et al. Design, fabrication, and modulation of THz bandpass metamaterials. *Laser Photonics Rev* **13**, 1900071 (2019).
52. Wu B, Jiang W, Jiang JQ et al. Wave manipulation in intelligent metamaterials: recent progress and prospects. *Adv Funct Mater* **34**, 2316745 (2024).
53. Chen CX, Kaj K, Zhao XG et al. On-demand terahertz surface wave generation with microelectromechanical-system-based metasurface. *Optica* **9**, 17–25 (2022).
54. Cong LQ, Pitchappa P, Lee C et al. Active phase transition via loss engineering in a terahertz MEMS metamaterial. *Adv Mater* **29**, 1700733 (2017).

Acknowledgements

The authors acknowledge the financial support from the National Key R&D Program of China (Nos. 2023YFB3811400, 2022YFB3806000), the National Natural Science Foundation of China (Nos. 12074314, 52202370, 52332006), the Aeronautical Science Foundation of China (No. 20230018053007), the Science and Technology New Star Program of Shaanxi Province (No. 2023KJXX-148), the Fundamental Research Funds for the Central Universities, and China Postdoctoral Science Foundation (No. 2023T160359).

Author contributions

Y. C. Fan, F. L. Zhang, Y. Z. Wen and J. Zhou conceived the idea and supervised the research. S. Q. Zhao and R. S. Yang designed, optimized and fabricated the metadevices structure. S. Q. Zhao, R. S. Yang and W. J. Luo performed the measurements. S. Q. Zhao wrote the paper. Z. H. Ye and C. Wang revised the paper. All authors commented on the manuscript.

Competing interests

The authors declare no competing financial interests.

Supplementary information

Supplementary information for this paper is available at https://doi.org/10.29026/oea.2025.240109

Scan for Article PDF